LA-UR- 98-3441

Approved for public release; distribution is unlimited.

Title: DAMAGE EVOLUTION AND CLUSTERING IN SHOCK LOADED TANTALUM

CONF-980768--

Author(s): W. R. THISSELL, MST-8
A. K. ZUREK, MST-8
J. M. RIVAS, MST-8
D. L. TONKS, X-NH
R. S. HIXSON, DX-1

Submitted to: 31st IMS Annual Convention
July 26-29, 1998
Ottawa

DISTRIBUTION OF THIS DOCUMENT IS UNLIMITED

MASTER

Los Alamos
NATIONAL LABORATORY

DISCLAIMER

DISCLAIMER

Portions of this document may be illegible in electronic image products. Images are produced from the best available original document.

Damage Evolution and Clustering In Shock Loaded Tantalum

W. R. Thissell[1], A. K. Zurek[1], J. M. Rivas[1], D. L. Tonks[2], and R. S. Hixson[3]

[1.] *Structure-Property Relationships, MS: G755*

[2.] *Nuclear Hydrodynamics, MS: F664*

[3.] *Detonation Science and Technology, MS: P952*

Los Alamos National Laboratory

Los Alamos NM 87545

www.lanl.gov

Two grades of tantalum were shock loaded by plate impact and recovered. The loading conditions were varied to study the damage evolution in the materials from incipient to full spallation. We performed quantitative image analysis and optical profilometry on the recovered specimens. Statistical analyses are shown of the void sizes, void clustering, and void linking in the two material grades.

Introduction

The ductile fracture process can be concisely described as the creation of a failure surface under the application of nominally mode I (tensile) loading by means of void nucleation and growth [1]. The nucleation, growth, and coalescence of voids characterize the mechanism of damage accumulation in ductile fracture. The origins of voids and their progressive accumulation at high strain rate loading are poorly understood for most materials. Void nucleation during deformation occurs most typically at interfaces, primarily at second-phase particles within a material, but also at grain boundaries, twin boundaries, and slip bands. Even pure materials contain impurities and inclusions that can act as nucleation sites. The particular manner in which the damage evolves, and hence the failure resistance of ductile materials, depends strongly upon the microstructure of the material, the strain rate, and the stress state.

Damage begins by a nucleation step, which can be defined as a de-cohesion between interfaces. These interfaces can be primarily second-phase particles, but also grain boundaries and twin boundaries. De-cohesion may be stress induced at intact particle interfaces, induced by particle cracking, or by strain induced dislocation pile-ups at particle-matrix interfaces or grain boundaries [2, 3]. The experimental validation of the parameters controlling de-cohesion in the dynamic loading regime is essentially non-existent. Once nucleated, void growth continues followed by coalescence and remote linking. Coalescence is when voids grow into each other until they intersect. Remote linking occurs when the stress and strain fields that surround each void begin to interact with that of their nearest neighbors and localized plastic yielding zones are created between voids. All of these steps are inherently statistical in nature. The applied stress state and strain rate profoundly influences the evolution of damage.

The ductile fracture process is therefore quite complex, containing several sequential and competing processes. Hence, micro- and meso-mechanical hydrocode models have been found to be very useful in developing a deeper understanding and predictive capability of these processes.

The pioneering work of Curran, Seaman, and Shockey [4-9] introduced quantitative descriptions of damage accumulation in dynamic incipient failure tests (plate impact, strain rates $> 10^5$, very large stress triaxialities, $-P/2\tau > 10$, where P is the mean stress and τ is the shear stress). They reduced their quantitative damage data to two empirical equations for nucleation and growth, and built hydrocode-based computational models for damage accumulation and dynamic ductile failure that included these equations. Several other models also exist, built around the modified Gurson failure surface [10-12], and incorporating the physics of void coalescence and linking [13].

This paper presents quantitative measurements of damage evolution in incipient spallation performed via flyer plate experiments [14]. The purpose of these measurements is to elucidate the microstructural mechanisms of damage accumulation at the meso-scopic length scale regime, ranging from 1 μm to 1 cm. The distillation of these measurements provides input data for, and validation of, meso-mechanical models of ductile fracture for hydrocode simulations [13, 15].

Materials

Two material grades of tantalum are compared, heretofore referred to as low purity and high purity. The impurity levels are shown in Table 1. It is not obvious by this table that the low purity material has in fact more impurities (interstitials, second phase particles) than the higher purity material. However, impurity chemistry is very difficult to perform on materials of this purity and refractory nature and are therefore prone to random errors. Recent studies of the strain hardening characteristics of these materials do support the labels provided [16, 17], as do our incipient fracture experiments described herein. The high purity material corresponds to the Ta material in the latter reference, and the low purity material is the material labeled Ta (10.2 mm) in the former reference. The low purity material has equiaxed grains of 48 μm average diameter while the high purity material also has equiaxed grains, but of 68 μm average diameter. Both materials have been annealed *in vacuo* at 1100 °C for one hour. Both materials have spall strengths that are dependent upon the strength of the incident shock. The higher purity material has a higher spall strength than the lower purity material.

Mechanical Testing

A flyer plate experiment is performed by launching a planar plate towards a planar target plate. Figure 1 is a *x-t* diagram of the experimental configuration employed in these tests. Planar impact results in two compressive shock waves traveling in opposite directions, one in the target and another in the flyer plate. The shock waves reflect from the free surfaces, becoming rarefraction waves. The intersection of the two rarefraction waves produces a region of almost pure hydrostatic tension that, in the absence of damage, reaches the same amplitude as the compressive shock stress. The accumulation of damage reduces the achievable tensile stresses. The strain rate of the tensile loading is on the order of 10^5 1/s, and the level of stress triaxiality, $-P/2\tau$, is typically > 10 (P is the hydrostatic or mean-normal stress, and τ is the flow stress).

The material subjected to the tensile loading has already been subjected to a compressive shock wave. Two significant changes occur to the material due to this compressive shock wave in comparison with the starting material. A significant number of lattice defects are introduced in the material. In metals, this can cause a strengthening effect similar to a uniaxial cold-working to 40-50 % strain, but without the grain distortion and texture evolution of uniaxial cold-working [18]. Brittle interfaces and second phases in the material can also crack under the influence of the compressive shock wave, thereby increasing the number density of easy damage nucleation sites.

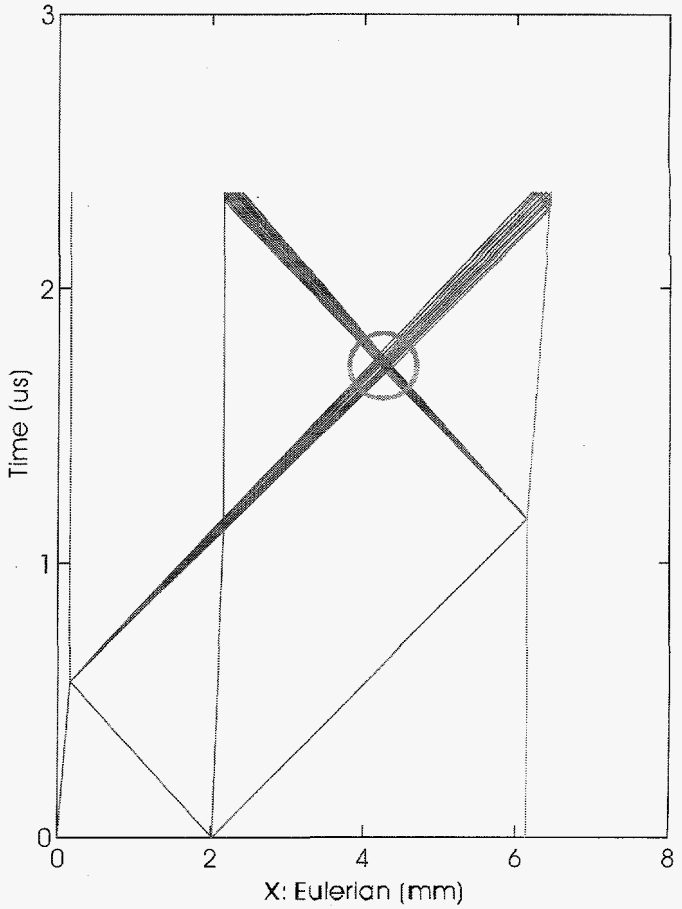

Figure 1: *x-t* diagram of the flyer plate experimental configuration used. Symmetric impact, ~2mm thick flyer plates impacting ~4 mm thick target plates. Red represents the compressive shock wave, blue represents the rarefraction fan, and the green circle highlights the region of tensile loading.

The tests were performed under incipient spallation loading conditions. This condition can be achieved by impacting at velocities insufficient to cause full fracture in the material. Pure uniaxial strain loading in the material is achieved by using momentum trapping rings, shown in Figure 4, to prevent the reloading of the sample by radial waves. The sample and inner ring are stripped from the outer ring after impact but prior to the return of the radial wave reflected from the outer surface of the outer ring. Soft sample recovery permits metallographic examination of the sample.

Table 1: Tantalum Impurity Levels, in ppm wt %

Material	Lab	C	N	O	H	Fe	Ni	Cr	W	Nb
Low Purity	Cabot	10	<10	<50	<5	<25	n/a	n/a	<25	<25
High Purity	NRC	6	24	56	<1	19	25	9	41	26

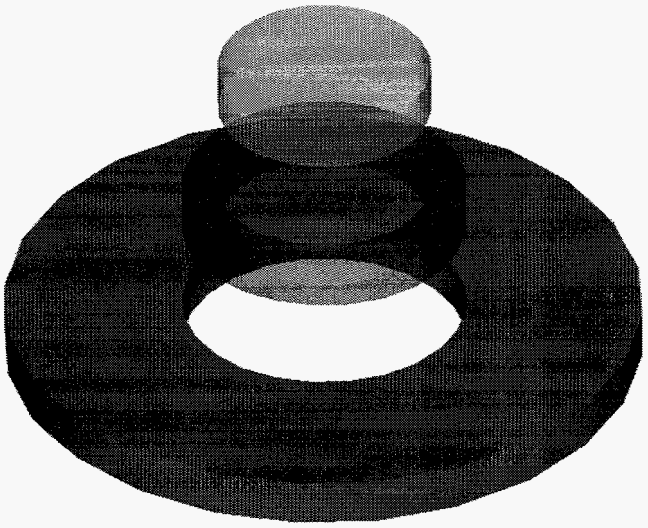

Figure 4: Exploded view of the momentum trapped sample design. The three parts are press-fit together. Green is the sample, blue is the inner momentum trap ring, red is the outer momentum trap ring.

We performed three incipiently spalled tests at approximately the same velocity of 252 m/s for the lower purity, and 245 m/s for the higher purity material. The tests capture the specimens at a different point along the failure path for each grade. Therefore, the following analysis provides an as yet incomplete study of the comparative damage accumulation phenomena of the two material grades. The two tests performed on the higher purity material included one in which the material was first pre-shocked with a 7 GPa compressive shock pulse to increase the initial concentration of lattice defects and easy void nucleation sites.

The back surface velocities of the samples were recorded using a velocity interferometer system for any reflector (VISAR) [19, 20]. Figure 3 compares the VISAR traces of the three tests. All three tests show pull-back characteristics that are substantially similar and do not indicate a very different dynamic fracture resistance.

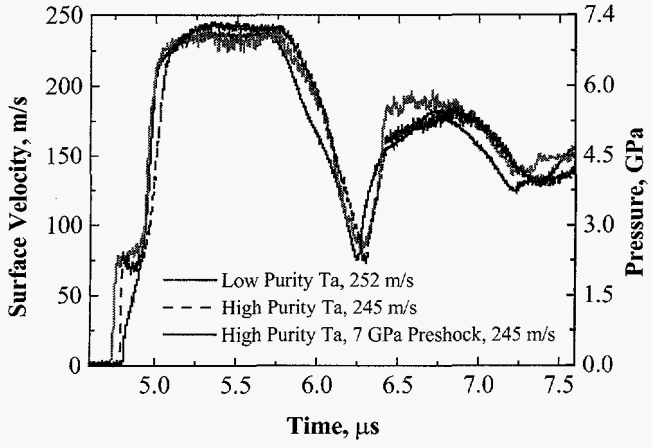

Figure 3: Back surface velocities of the samples.

Metallography

The recovered specimens were sectioned parallel to the direction of shock wave propagation, polished, and lightly etched using Kelly's etch [21]. Figure 2 shows the

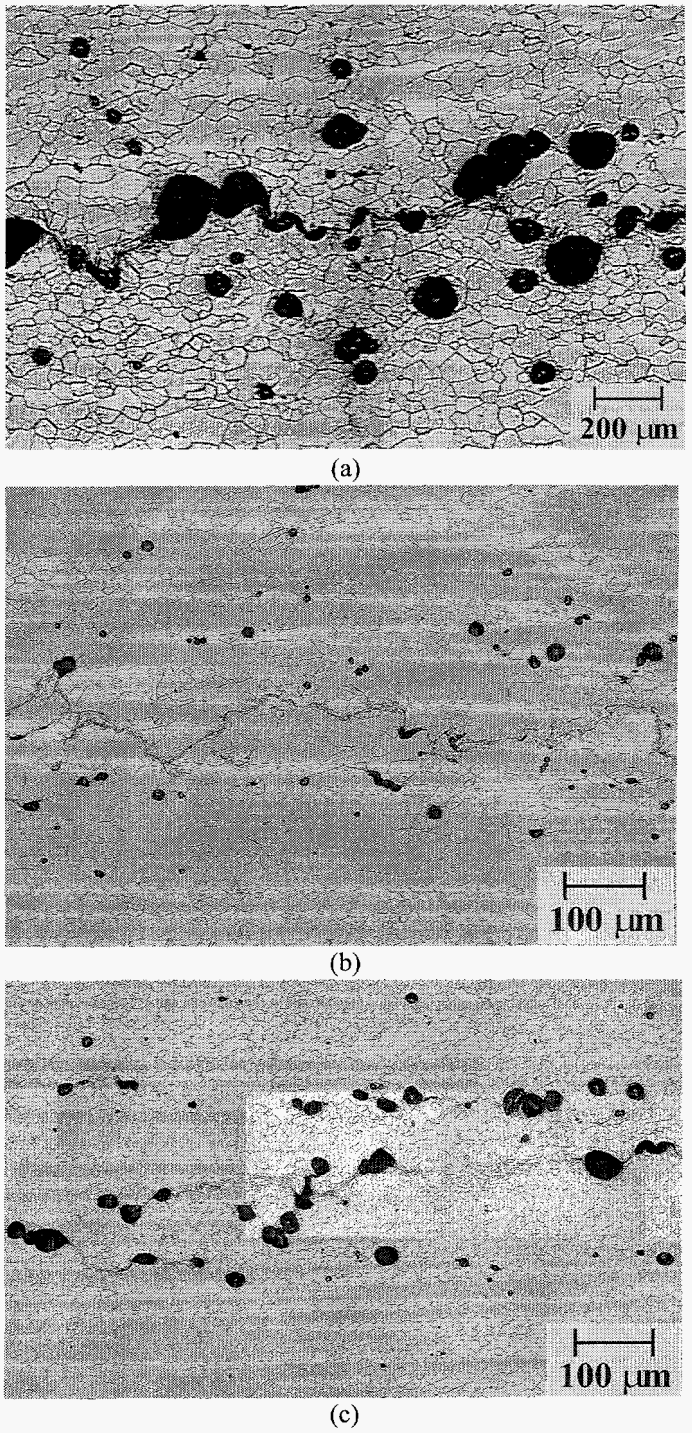

Figure 2: Metallography of the recovered specimens. (a) is the low purity material impacted at 252 m/s; (b) is the high purity material impacted at 245 m/s; (c) is the high purity material pre-shocked at 7 GPa and impacted at 245 m/s. The darker curves connecting voids are regions of etch revealed plasticity linking the voids.

microstructures of the recovered specimens. Qualitatively, very large differences are evident. The higher purity material has fewer and smaller voids, but more and longer plastic linking ranges, than the lower purity material. The preshocked specimen exhibits intermediate behavior in these aspects compared to the other two tests.

Quantitative Analysis

We performed three-dimensional quantitative measurements of the microstructural damage using image analysis and optical profilometry. The details have been previously described [22, 23]. The technique provides a sampling of the true sizes of voids intersecting the section plane. The measurements obtained include the average diameter, area, aspect ratio, void depth from the section plane, and planar centroid location, from which the true void size and three-dimensional centroid location was reconstructed assuming spherical voids.

Solid Models of Damage

The damage data can be represented as a solid model to more easily understand its three-dimensional character. The ACIS® format provides data portability and the ability to readily rotate, pan, and zoom the model on a computer, thereby providing an important means to visually inspect and debug the data for validity.

Figure 5 shows isometric views of the quantified damage within the three specimens. The lower purity material exhibits a rather homogeneous distribution of voids and clusters across the specimen length, with much less void linking than the higher purity material. The higher purity material specimens show larger voids and clusters at the periphery of the specimens, this is especially pronounced in the specimen that was not pre-shocked.

Sample Assembly Design Effects

Recovery spallation experiments require very careful sample assembly design in order to achieve true uniaxial strain loading conditions across the entire specimen and to have proper specimen release and recovery without introducing significant additional sample loading. Both material purity grades were tested with the momentum rings consisting of the lower purity material, annealed identically to the specimen.

We have studied the influence of the momentum trapping material on the spall behavior. The micrographs do indicate that the higher purity material has larger voids at the periphery than the lower purity material, but the solid models, constructed using the true void diameters, really make the difference apparent. Figure 6 shows bivariate scatter plots of void size versus position along the specimen of the low purity and high purity material tests. It is quite clear from these graphs that the momentum trap design does a marvelous job of achieving a homogeneous loading history across the entire specimen, when the momentum rings are constructed of material identical to the sample material. However, even the slight material differences between the two different material grades reported here have a significant impact on the loading history across the specimen. The observable effect of the different material purity of the

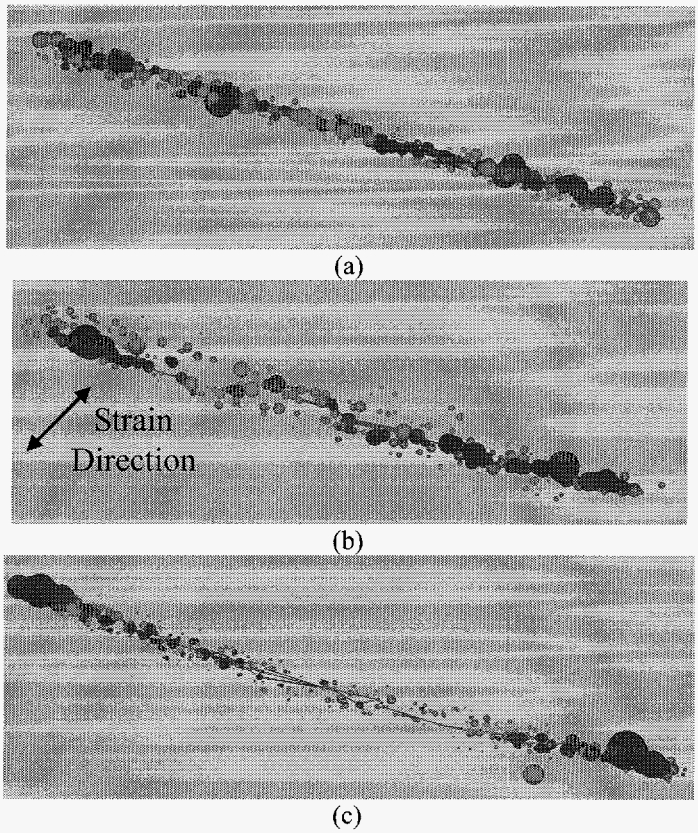

Figure 5: Isometric solid modeling representations of damage. Green is for an isolated void, blue is for a cluster, and red indicates a linking range. (a) lower purity Ta, shot at 252 m/s; (b) higher purity Ta, pre-shocked at 7 GPa, shot at 245 m/s; (c) higher purity Ta, shot at 245 m/s.

momentum trapping rings on the high purity material test is to increase the maximum observable size of the voids and to increase their clustering in the region proximate to the boundary between the material grades. However, the smaller voids in periphery of the sample occur in approximately the same number density and sizes as the material in the center of the sample specimen.

Decreasing the sampled area to the sample material dominated region decreases the number of observations to the extent that a significant statistical representation is not achieved.

The following analysis uses the sample material dominated regime for the porosity calculations and the entire specimen length for the other analyses.

Aspect Ratio Analysis

A central test of the appropriateness of our simplification to spherical voids is a quantification of aspect ratios. The definition of aspect ratio used is the ratio of the major to minor axis lengths of an ellipse equivalent to the object, *i.e.*, same area and first and second degree moments. Figure 7 shows plots of the cumulative percentage of aspect ratios for the three tests, as well as gamma distribution fits to the data. The gamma distribution well describes all the observations for the low purity test, and about 80 % of the observations in the high purity tests. Almost all of the observations with aspect ratios above two are

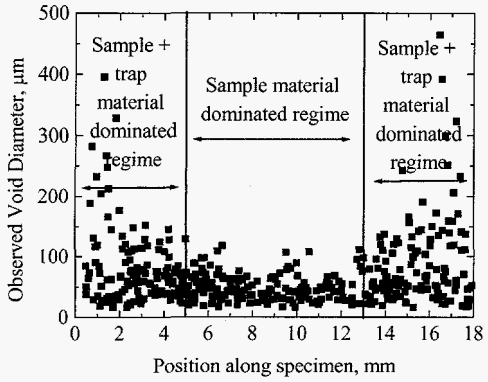

(a)

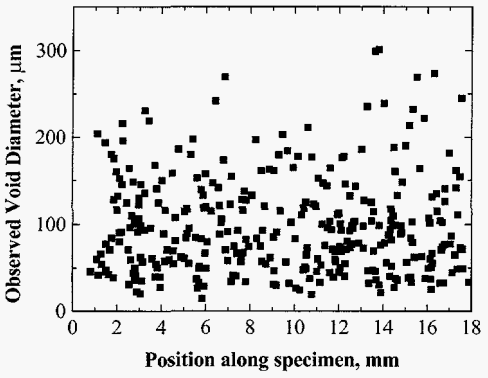

(b)

Figure 6: Observed true void sizes versus position along the sampling plane in the direction perpendicular to the shock loading direction and parallel to the plane of maximum porosity for (a) the high purity test, and (b), the low purity test.

associated with opening linking ranges, while aspect ratios of two or less are usually isolated voids or cluster members. Again we therefore see an artifact of a difference of linking range behavior due to material purity and initial dislocation concentration that we attribute to a difference in flow stress. Figure 8 shows a micrograph of the high purity test which shows several opening linking ranges, each having aspect ratios larger than two. In conclusion, we deem the simplification to spherical voids to be very well justified for the low purity test, and adequate for an initial quantification effort for the high purity tests.

Porosity

The porosity was calculated using quantified void data and is shown in Figure 9. The low purity test has a rather smoothly varying porosity compared to the other two tests where the sampled area was decreased to the sample material dominated regime. The definition of the incipient spall plane is the plane of maximum porosity. The fluctuations in porosity that are evident in the high purity material tests are attributed to the lower porosity and smaller sampled area. The damage has progressed to almost final failure in the low purity test, usually defined as

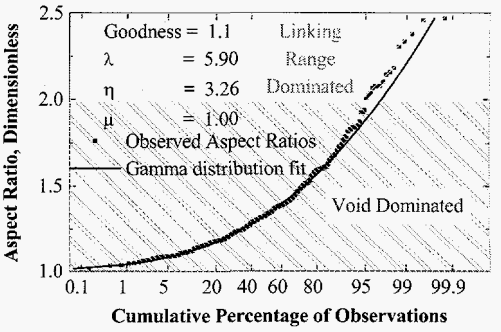

(a)

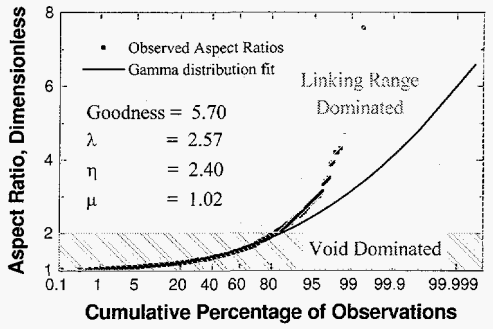

(b)

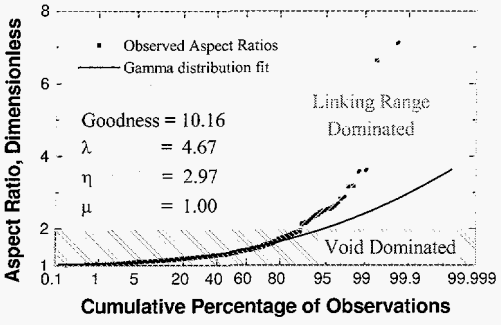

(c)

Figure 7: Aspect ratio comparison for the voids: (a) low purity; (b) high purity test; and (c) pre-shocked.

30 % porosity, while the high purity test had progressed to only about 5 % porosity.

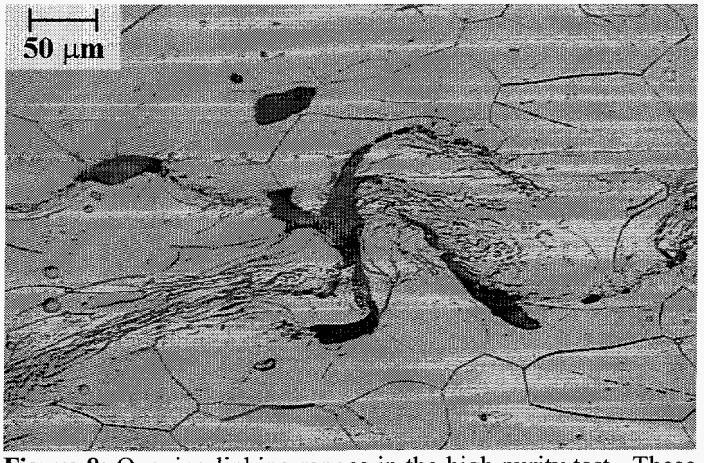

Figure 8: Opening linking ranges in the high purity test. These have an aspect ratio larger than two.

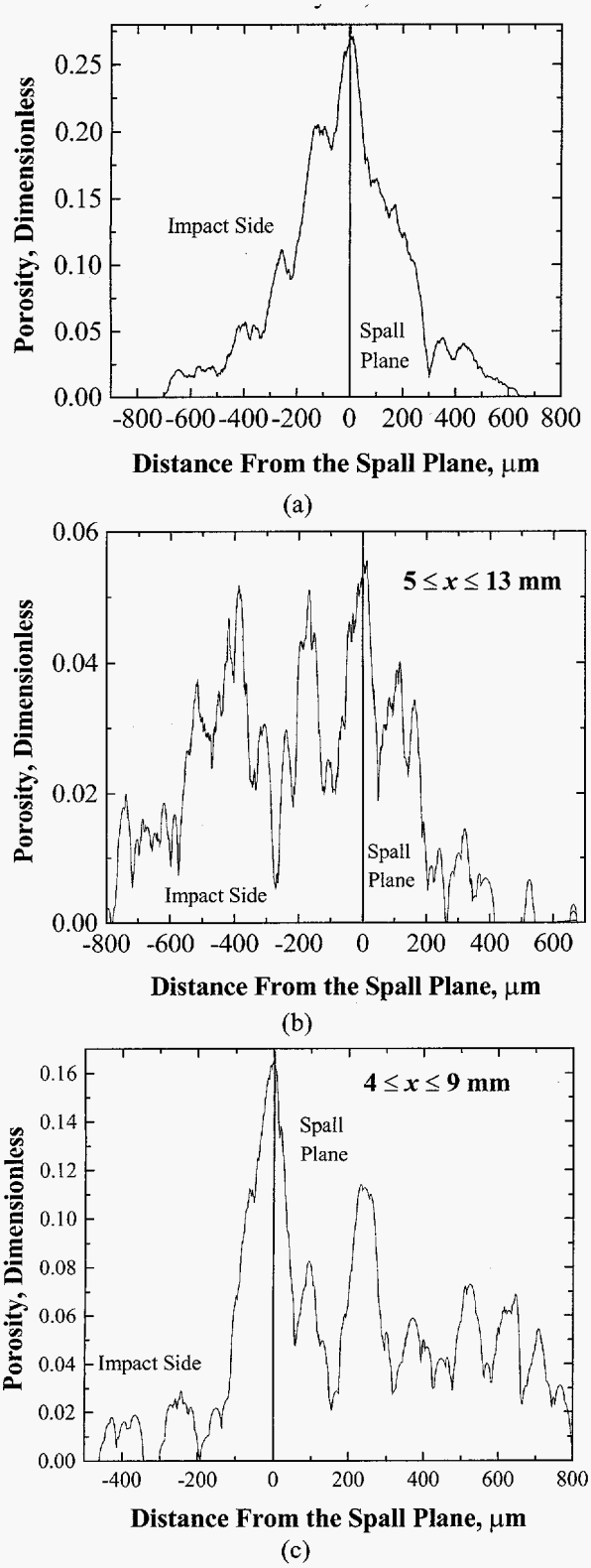

Figure 9: Porosity calculations from the quantified void data. (a) the low purity test; (b) the high purity test; (c) the 7 GPa preshocked high purity test. The two latter graphs are of the sample material dominated regime.

Void Size Distributions

The planar sampling section plane skews the observations of the volumetric void distribution such that smaller voids are underrepresented whilst the larger voids are over represented [23]. The true volumetric void size distribution can be determined once a probability distribution has been found to describe the observed void sizes.

The results of the observed and true volumetric size distributions are shown in Figure 10 for the cumulative distribution. Figure 10 compares the two-dimensional (base) diameter measurements with the true three- dimensional measurements obtained by combining the optical profilometer data with the image analysis obtained measurements. The void sizes in all three tests can be well described by either a log-normal distribution, or by a linear combination of a Weibull (for the smaller sizes) and a log-normal for the larger void sizes. The advantage of the latter distribution function is that is bounded at the lower end, a condition suitable for high levels of stress triaxiality in materials that exhibit nucleation dominated failure behavior. The cumulative true volumetric distributions indicate smaller voids than the 2-D (base) observations indicate, and the shape of the distribution is different. This is attributed to the fact that the actual distribution of voids is not uniform, and hence the 2-D (base) cumulative distribution is not Gaussian. The true median diameter ranges from 60-70 % of the observed median size for the three tests. But, the shape of the true void size distribution can differ substantially from the observed void size distribution. Table 2 lists a summary of the data shown in Figure 10.

Coalescence: Clusters and Linking

The third stage of the ductile fracture process is damage coalescence to form the failure surfaces. Coalescence occurs via voids growing into each other forming void clusters, and by plastic instabilities due to the enhanced stress and strain fields between voids. The quantification of void centroids and true sizes permit a statistical analysis of void clustering and linking.

We have approximated void clusters as rectangles, with a cluster length corresponding to the edge to edge length of the cluster. The cluster area is equal to the average cluster member diameter times the cluster length. Two voids are assumed to be a cluster when the edge to edge distance between them is < 1/10 the diameter of the small void.

Figure 11 compares the observed cluster lengths and areas for the three tests. Both cluster lengths and areas are reasonably described by a log-normal distribution. The median cluster lengths are about 230, 210, and 135 μm for the low purity, pre-shocked, and high purity tests, respectively. The median cluster areas are about 27,500, 19,000, and 10,500 μm^2, in the same order. This follows a similar trend as the void sizes for the three specimens. The number of voids that are cluster members are 120, 100, and 168, for the low purity, pre-shocked, and high purity tests.

Linking ranges are more difficult to describe statistically. A preliminary comparative analysis is shown in Figure 12. About 80 % of the linking range observations can be well described by a gamma distribution. The gamma distribution is often used to

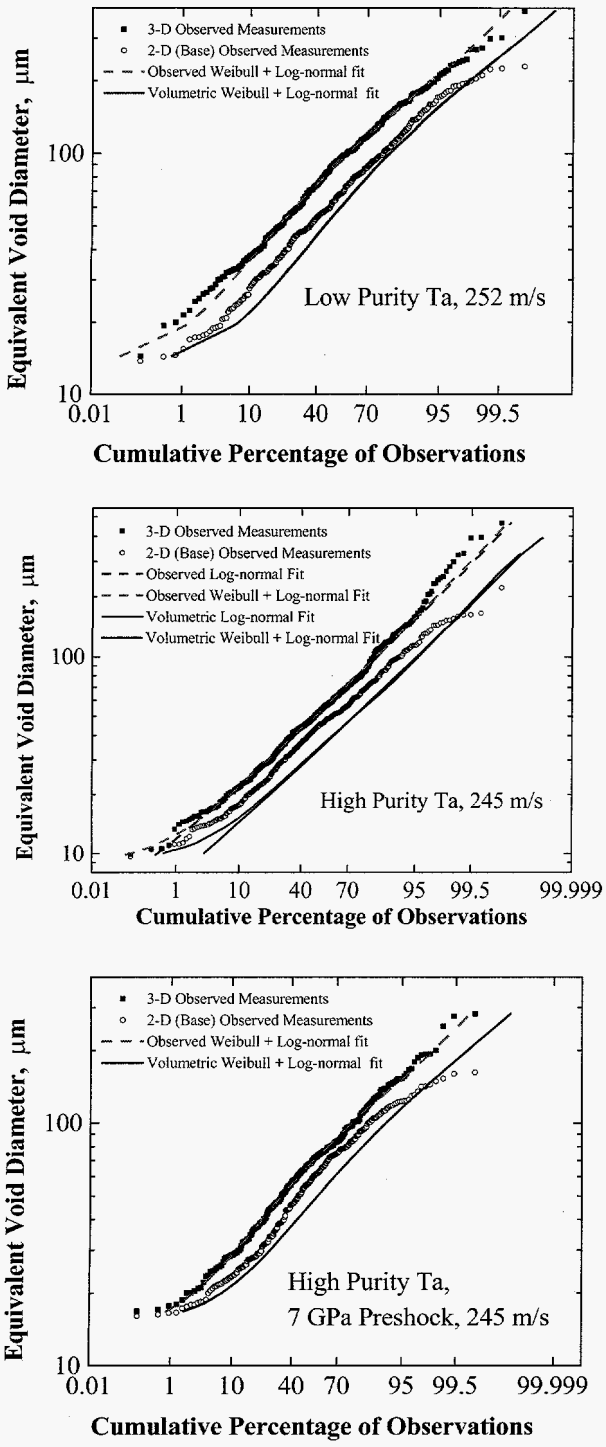

Figure 10: Cumulative percentage of observation plots of the void sizes for the three tests.

describe random variables bounded at one end. The ordinate for these plots is the edge to edge distance of the two voids, calculated in the plane connecting their centroids bounding the linking range divided by the mean of their true void diameters.

A couple of linking ranges for each sample had values slightly smaller than zero because the plane connecting the voids' centroids was different from the section plane upon which the linking range was observed. The program will be changed such that the edge to edge distance will be calculated using the section plane.

The high purity test showed significantly more linking ranges than either the pre-shocked and the low purity test. Seventy percent of the linking ranges in each test were within the average void diameter of each other.

One explanation for why this analysis is less satisfying than the other analyses described previously is that we are not capturing the tortuosity of the linking ranges. Figure 13 shows a micrograph from the high purity test that contains numerous linking ranges, the central one exhibiting extensive tortuosity. The long linking ranges show much more extensive tortuosity than the shorter ones. The very long linking ranges could also be connecting within their length voids that do not intersect the section plane and hence are not observed. However, since the linking ranges in the section plane are typically only about 1/5-1/8 as wide as the linking void diameters, linking to voids outside the section plane would result in linking ranges that do not appear to be bounded by voids.

Summary

The preliminary damage quantification analysis presented here shows that significant differences exist in porosity, void sizes, clustering, and linking behavior among the three tests that are not collaborated by the VISAR free surface velocity traces. This is explained by the fact that the damage processes are occurring in a small region at the center of the sample thickness, while the VISAR samples the back surface velocity. The effect that the evolving damage has on the particle velocity must propagate through essentially ½ the sample thickness to be detected by the VISAR and is to a large extent masked by the larger scale particle velocity effects of the test.

The pronounced linking that is especially evident in the high purity test is attributed to the higher level of tensile hydrostatic stress achieved in this specimen due to the smaller level of porosity.

The determination of physically based void growth and nucleation relations is made more complicated by the linking between tensile loading and damage evolution

Table 2: Summary of Void Size Analysis

	Low Purity Ta, 252 m/s		High Purity Ta, 245 m/s		High Purity Ta, Preshocked, 245 m/s	
Parameter	Observed	True	Observed	True	Observed	True
N	326		475		266	
Median Diameter, μm:	**88**	**55**	**51**	**33**	**65**	**44**

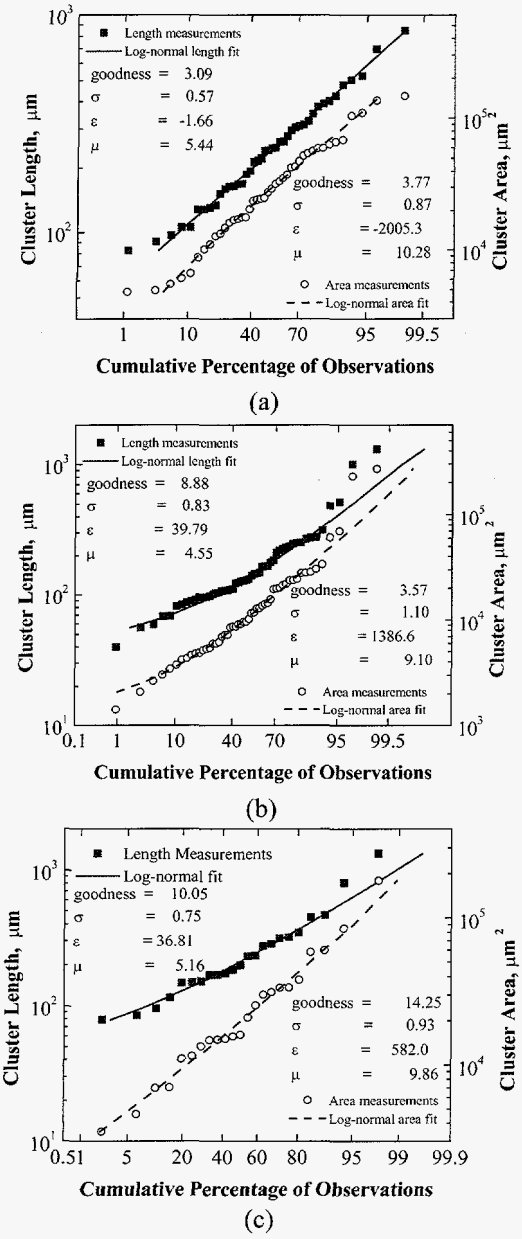

Figure 11: Cluster analysis comparison. (a) low purity, $N = 42$, (b) high purity, $N = 53$, and (c) pre-shocked, $N = 23$.

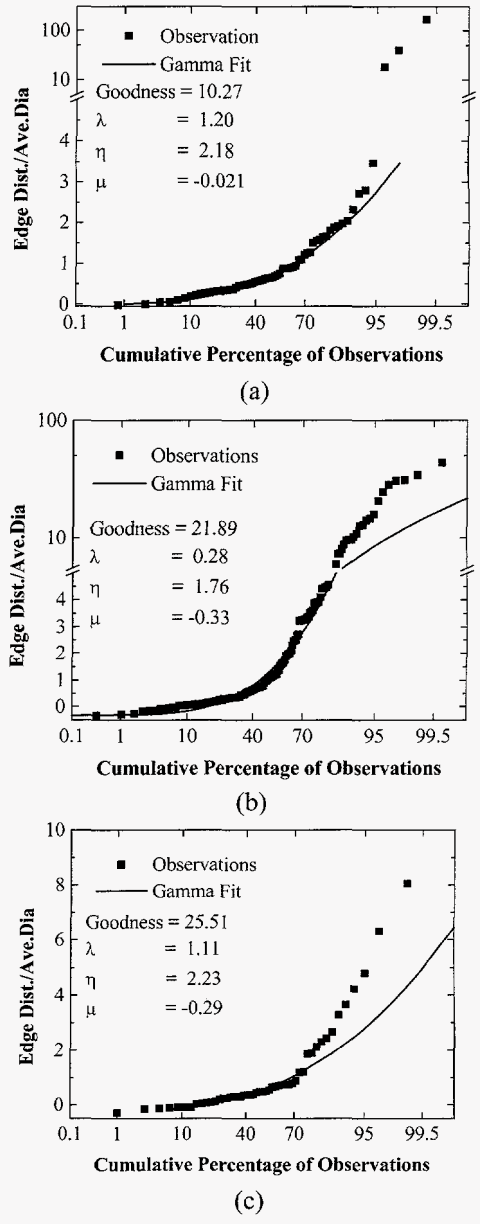

Figure 12: Linking range analysis comparison. (a) low purity, $N = 65$, (b) high purity, $N = 143$, and (c) pre-shocked, $N = 50$.

Figure 13: A tortuous linking range in the high purity test. This micrograph has numerous linking ranges, several of which are exiting the boundaries of the micrograph.

Acknowledgements

The authors thank Carl Trujillo for performing the spall experiments. David Embury and Jim Johnson are thanked for their comments. This project is sponsored by the Joint DoD/ DOE Munitions Program.

References

[1] P. F. Thomason, Ductile Fracture of Metals, Pergamon Press, New York, (1990).

[2] A. S. Argon and J. Im, Metallurgical Transactions A, 6A, 839-51, (April 1975).

[3] A. S. Argon, J. Im, and R. Safoglu, Metallurgical Transactions A, 6A, 825-37, (April 1975).

[4] T. W. Barbee, Jr., L. Seaman, R. Crewdson, et al., Journal of Materials, 7, 3, 393-401, (September 1972).

[5] D. R. Curran, L. Seaman, and D. A. Shockey, Physics Reports, 147, 5&6, 253-388, (1987).

[6] D. R. Curran, L. Seaman, and D. A. Shockey, Physics Today, 46-55, (January 1977).

[7] L. Seaman, Donald A. Shockey, and Donald R. Curran, in International Conference on Dynamic Crack Propagation, edited by G. C. Sih (Noordhoff International Publishing, Groningen, Netherlands, Bethlehem, PA, July 10-12, 1972), p. 629-47.

[8] L. Seaman, D. R. Curran, and D. A. Shockey, Journal of Applied Physics, 47, 11, 4814-26, (November 1976).

[9] L. Seaman, D. R. Curran, and R. C. Crewdson, Journal of Applied Physics, 49, 10, 5221-9, (October 1978).

[10] J. N. Johnson and F. L. Addessio, Journal of Applied Physics, 64, 12, 6699-712, (December 15, 1988).

[11] J. N. Johnson, J. of Applied Physics, 52, 4, 2812-25, (1981).

[12] Q. H. Zuo, F. L. Addessio, and P. J. Maudlin, (Los Alamos National Laboratory, Los Alamos, New Mexico, 87545, 1998), 1-16.

[13] D. L. Tonks, A. K. Zurek, and W. R. Thissell, in Metallurgical and Materials Applications of Shock-Wave and High-Strain-Rate Phenomena (EXPLOMET'95), edited by L. E. Murr, K. P. Staudhammer and M. A. Meyers (Elsevier, New York, 1995), p. 171-8.

[14] M. A. Meyers, Dynamic Behavior of Materials, John Wiley & Sons, Inc., New York, (1994).

[15] D. L. Tonks, in Dynamic Plasticity and Structural Behaviors, edited by S. Tanimura and A. S. Khan (Gordon and Breach, Luxembourg, 1995), p. 119-22.

[16] S. R. Chen and G. T. Gray, Metallurgical and Materials Transactions a-Physical Metallurgy and Materials Science, 27, #10, 2994-3006, (1996).

[17] G. T. Gray, III and K. S. Vecchio, Metallurgica and Materials Transactions A, 26, 2555-63, (October 1995).

[18] G. T. Gray, III, in High-Pressure Shock Compression of Solids, edited by J. R. Asay and M. Shahinpoor (Springer-Verlag, New York, 1993), p. 186-215.

[19] L. M. Baker and R. E. Hollenbach, J. Applied Physics, 43, 11, 4669-75, (1972).

[20] W. F. Hemsing, Review of Scientific Instruments, 50, 1, 73-8, (January 1979).

[21] A. M. Kelly, S. R. Bingert, and R. D. Reiswig, Microstructural Science, 23, 185-95, (1996).

[22] A. K. Zurek, W. R. Thissell, D. L. Tonks, R. Hixson, and F. Addessio, Journal de Physique Colloque C3, 903-8, (1997).

[23] W. R. Thissell, A. K. Zurek, D. L. Tonks, et al., in 21st International Symposium on Shock Waves, edited by A. F. P. Houwing, Great Keppel Island, (1997), paper 6880.